JOURNAL OF MATERIALS SCIENCE **40** (2005) 6071 – 6077

Modelling of solidification of Ti-45 at%Al alloy ingot by the stochastic model

LIU DONG-RONG, WU SHI-PING, GUO JING-JIE, SU YAN-QING, FU HENG-ZHI
School of Materials Science and Engineering, Harbin Institute of Technology, Harbin 150001, People's Republic of China
E-mail: hlgldr@163.net

Published online: 24 October 2005

A comprehensive stochastic model for simulating grain structure formation and evolution during solidification processes is developed, based on a finite differential method (FDM) for macroscopic heat flow calculation and a cellular automaton method (CA) for microscopic modelling of nucleation, growth, solute redistribution and solute diffusion. Formation of peritectic phases in the last solidified liquid regions is considered. The growth rates of peritectic phases are calculated by the peritectic growth kinetics model. The solidification contraction is also taken into account. The calculated results are compared with those obtained experimentally.

1. Introduction

Ti-Al alloy exhibits a remarkable potential for structural applications in aerospace and automotive industries at high temperatures. During the last decade, research and development of this alloy was focused on a better understanding of the grain structure formation. Then, a quantitative study and control of solidification sequences in casting is important since it is closely related to the productivity of the process and the quality of the casting products. Therefore, there is a considerable potential for using computer simulation as a tool for this purpose.

Deterministic models have been first developed for the description of the nucleation, growth and impingement of equiaxed grains during solidification processes [1]. However these models suffer from several limitations [2]: (1) the grains are assumed to remain spherical even in a strong thermal gradient; (2) columnar structures and thus the columnar-to-equiaxed transition (CET) are usually not accounted for; (3) the competition occurring among the grains belonging to the columnar zone and the associated evolution of their crystallographic texture are not described at all; (4) simulated micrographs cannot be produced using such models.

Stochastic models have been developed to solve the limitations mentioned above, by which individual grains are identified and their shape and size can be shown graphically. Spittle and Brown [3] used a Monte Carlo (MC) method to simulate grain growth and grain interaction during solidification. The influence of processing variables on grain structure in a single-phase binary alloy was studied. However, MC method ignores the specifics of dendrite growth that include tip kinetics and preferred crystallographic growth direction, and therefore suffers from a lack of physical background. Rappaz and Gandin [4] first used the Cellular Automaton-Finite Element (CA-FE) technique to predict solidification grain structures in turbine blade casting. The heterogeneous nucleation, the growth kinetics and the preferential growth directions of dendrites were taken into account in their model. However this technique suffers from one limitation: in the calculation for equiaxed dendritic solidification, constant growth coefficient was assumed. The influence of microsegregation on solidification grain structure is ignored. In the model developed by Nastac and Stefanescu [5], the effect of microsegregation on solidification was included through the correct calculation of the equiaxed dendritic growth coefficient. And the size and shape of grains predicted by this model were in better agreement with the experimental observations. But the calculation of microsegregation is performed in a complex deterministic way [6] and not proper for efficient simulation of grain structure formation in the real castings. Tongmin Wang *et al.* [7] developed a modified cellular automaton (MCA) method, in which solute redistribution and solute diffusion were coupled with microscopic nucleation and growth of grains. Howerver, due to the consideration of microsegregation in the MCA, how to deal with the last solidified liquid regions is not explained in their model. Furthermore, the solidification contraction occurring during solidification processes is also ignored.

In this paper, a comprehensive stochastic model for simulating grain structure formation is developed, based on the FDM method for macroscopic modelling of heat transfer and a CA method for microscopic modelling of nucleation, growth, solute redistribution and solute diffusion. For Ti-45 at%Al alloy, the formation of peritectic phases in the last solidified liquid regions is considered. The growth rates of peritectic phases are

0022–2461
DOI: 10.1007/s10853-005-0841-2

calculated by the peritectic growth kinetics model. The solidification contraction is also taken into account. The simulated results are compared with those obtained experimentally.

2. Mathematical model

2.1. Governing equations

We solve the heat equation by means of the finite-difference method.

$$\rho c_p \frac{\partial T}{\partial t} = \nabla(\lambda_L \nabla T) + \rho L \frac{\partial f_s}{\partial t} \tag{1}$$

where λ_L is the liquid thermal conductivity; ρ is the density; c_p is the specific heat; L is the latent heat; and f_s is solid fraction.

For the solution of Equation 1, provided that the increase in solid fraction at each node, $\Delta f_{s,i}$, is known, the new temperature is given by:

$$T_i^{t+\Delta t} = T_i^t + \frac{\lambda_L}{\rho c_p}\nabla(\nabla T)\Delta t + \frac{L}{\rho c_p}\Delta f_{s,i} \tag{2}$$

where i is a subscript indicating the different nodes of the FDM mesh. The role of the stochastic method is to provide the change in solid fraction, $\Delta f_{s,i}$, at each node during each time step, from which new temperature can be calculated. The coupling between the macroscopic heat diffusion and microscopic microstructural evolution takes place through Equation 2.

It is assumed that local equilibrium at the solid/liquid interface:

$$C_S^* = kC_L^* \tag{3}$$

where k is the partition coefficient; C_S^* is solid concentration at S/L interface; and C_L^* is liquid concentration at S/L interface.

Solute diffusion in a binary system is given by:

$$\frac{\partial C_L}{\partial t} = D_L \nabla(\nabla C_L) \tag{4}$$

where D_L is the liquid diffusion coefficient; C_L is the liquid concentration, no solute diffusion in the solid.

2.2. Nucleation model

Gaussian law is used in the continuous nucleation model:

$$\frac{dn}{d(\Delta T)} = \frac{n_{\max}}{\sqrt{2\pi}\cdot\Delta T_\sigma}\exp\left(-\frac{(\Delta T - \Delta T_{\max})^2}{2\cdot\Delta T_\sigma^2}\right) \tag{5}$$

where n is the nuclei density; $n_{\max}$ is the maximum nuclei density; ΔT_σ and $\Delta T_{\max}$ are the standard deviation and the mean nucleation undercooling of the distribution.

2.3. Growth model

For the case of columnar dendritic solidification, the Kurz-Giovanola-Trivedi (KGT) model [8] is used to calculate the growth rate:

$$V_{\text{columnar}} = A(\Delta T)^2 = \frac{D_L}{2\pi^2 m\,(k-1)C_o\Gamma}\,(m(C_o - C_L^*))^2 \tag{6}$$

where A is growth coefficient; Γ is the Gibbs-Thomson coefficient; m is the liquidus slope and ΔT is the undercooling.

For equiaxed dendritic solidification, the model developed by Nastac and Stefanescu [5] is applied. Thus, the growth velocity of the tip is described by:

$$V_{\text{equiaxed}} = B(\Delta T)^2 \quad \text{with} \quad B = \frac{2\sigma^*}{\Gamma}\left[\frac{m(k-1)C_L^*}{D_L} + \frac{\rho L}{\lambda_L}\right]^{-1} \tag{7}$$

where B is growth coefficient and $\sigma^* = 1/4\pi^2$. The melt undercooling for the system under consideration can be calculated based on the following assumption:

$$\Delta T = TL + m(\langle C_L\rangle^L - C_o) - T_b \tag{8}$$

where TL is the equilibrium liquidus temperature; $\langle C_L\rangle^L$ is the intrinsic volume average extradendritic liquid concentration and T_b is the average temperature in the macro-element. For the growth of peritectic phase, the growth kinetics model is developed by Fredrikson *et al.* [9]:

$$V_p = \frac{9}{8\pi}\frac{D_L}{R}\Omega_p^2 \tag{9}$$

$$\Omega_p = \frac{\Omega^{*2}}{5.6\left(1 - \frac{2}{\pi}\Omega^* - \frac{1}{2\pi}\Omega^{*2}\right)} \tag{10}$$

$$\Omega^* = \frac{C_L^{\alpha\text{-Ti}} - C_{PL}}{C_L^{\alpha\text{-Ti}} - C_{\alpha\text{-Ti}}^L} \tag{11}$$

$$R = \frac{32R_c}{3\Omega^*} \tag{12}$$

$$\Delta T_p = m_{\alpha\text{-Ti}}^L C_{PL}\frac{(1-k_{\alpha\text{-Ti}})\Omega^*}{1-(1-k_{\alpha\text{-Ti}})\Omega^*} \tag{13}$$

where Ω_p is function of peritectic-solute supersaturation; Ω^* is peritectic-solute supersaturation; For Ti-45 at%Al alloy, $C_L^{\alpha\text{-Ti}}$ and $C_{\alpha\text{-Ti}}^L$ are liquid concentration and solid concentration of α-Ti in equilibrium, respectively; R is the actual tip radius; R_c is the critical radius for nucleation (1 μm). From Equations 9–13, no simple relationship between growth rate V_p and undercooling ΔT_p can be obtained. Then, a numerical solution, approximated by an exponential function, is developed:

$$V_p = C \times \exp\left(\frac{\Delta T_p}{D}\right) \quad \text{with} \quad C = 2.8\times10^{-6} \qquad D = 1.02 \tag{14}$$

where C and D are growth constants.

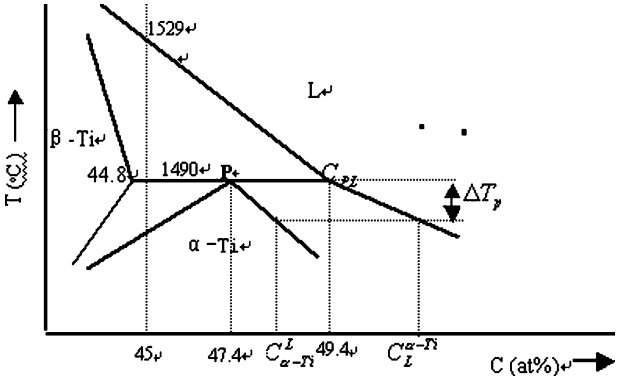

Figure 1 Phase diagram of Ti-Al alloy.

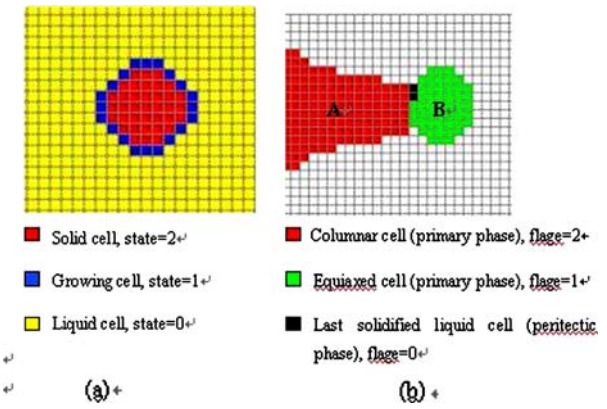

Figure 2 The schematic illustration of CA lattice: (a) solidification state and (b) phase state of cell.

Fig. 1 shows the phase diagram of Ti-Al alloy [10].

2.4. Solid fraction

During growth, a cell generates a microscopic increase in solid fraction equal to:

$$\delta f^t_{s,\text{cell}} = \frac{V\Delta t}{\Delta x} \tag{15}$$

where V is growth rate; Δt is time step; and Δx is the cell size. At each node of the finite-difference mesh, the microscopic contributions are added and give rise, at the end of the loop over all grains, to the macroscopic increases of solid fraction at each node of the FDM mesh during the time step. It is this macroscopic $\Delta f_{s,i}$ that is used in the heat balance Equation 2 to determine the new temperature.

3. Formation of the shrinkage cavity

Due to the consideration of the solidification contraction, the formation of the shrinkage cavity at the top of the ingot is taken into account. The total shrinkage volume (including liquid shrinkage and solidification contraction) is calculated after each time step Δt and summed. Once the shrinkage volume exceeds the volume of a macro-element that (1) contains Ti-45 at% alloy; (2) has a solid fraction less than 0.4 and (3) is closest to the top or a top-solidified shell, that the macro-element is considered empty and a new summation is started. Properties of an empty macro-element are taken to be those of the insulating powder [11]. In this paper, the liquid shrinkage coefficient β_L and solidification contraction coefficient β_S are taken as 9%/100°C and 4.42%, respectively.

4. CA modelling

A CA is a dynamical system in which space, time and states of the system are discrete. Each cell in the regular spatial lattice can be in any one of a finite number of states. The rules of transition, which determine the evolution of a given cell during one time step, are defined according to the states of its neighbor cells. Therefore, for the CA modelling, the following rules must be preliminarily determined [12]: (1) the neighborhood of a cell; (2) the solidification state of cells (liquid or growing or solid); (3) the rule of nucleation; (4) the rule of growth; (5) rule of solute redistribution and solute diffusion and (6) the time step.

Fig. 2 is a schematic representation of CA lattice with a two-dimensional square enmeshment of cells. In this paper, the rules of transition are:

(1) 4-cell neighborhood;
(2) three states for a cell: liquid or growing or solid, as shown in Fig. 2a;
(3) the number of nuclei is calculated by continuous nucleation model and nucleation sites are distributed randomly among the liquid cells with the local undercooling larger than the prescribed nucleation undercooling;
(4) a solidified cell ($fs = 1$) will turn its neighboring liquid cells into growing cells and for growth to occur, a cell should be at a temperature below the liquidus temperature for the cell concentration $C_{L,\text{growing\_cell}}$ and the growth probabilistic coefficient be larger than a randomly generated number (0–1). The growth rates of the columnar and the equiaxed are calculated by different growth models. For Ti-45 at%Al alloy, when temperature of a growing cell is lower than the peritectic temperature and solid fraction of it smaller than 1, the cell will solidify as the peritectic phase and the growth rate is calculated by peritectic growth kinetics model. The phase state for a cell is shown in Fig. 2b.
(5) if a cell solidifies, it will reject the excess solute to its neighboring liquid cells and turn them into growing cells. Then, the liquid concentration $C_{\text{L,growing\_cell}}$ for the neighboring liquid cells is:

$$C_{L,\text{growing\_cell}} = C_{L,\text{growing\_cell}} + \frac{C^*_{L,\text{solidified\_cell}}(1-k)}{Num} \tag{16}$$

where Num is the number of neighboring liquid cells and $C^*_{L,\text{solidified\_cell}}(1-k)$ is the excess solute rejected by the solidified cell. Solute diffusion is performed between the growing cells and the liquid cells by Equation 4. For the calculation of $\langle C_L \rangle^L$, the following

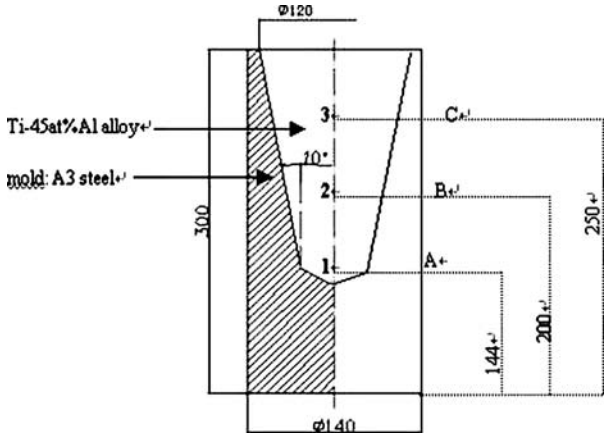

Figure 3 The schematic diagram of the ingot and mold.

equation is used:

$$\langle C_L \rangle^L = \frac{\sum_{i=1}^{Num1} C_{L,\text{liquid\_cell},i}}{Num1} \tag{17}$$

where $Num1$ is the number of liquid cells in one macro-element and $C_{L,\text{liquid\_cell}}$ is the liquid concentration for the liquid cell.

(6) the growth of the dendritic network during one time-step cannot exceed the cell spacing.

5. Results and discussion

The present stochastic model is applied to simulate the grain structure formation and evolution during the solidification processes of Ti-45 at%Al alloy ingot. The schematic of the two-dimensional ingot vertical section is shown in Fig. 3, where all dimensions are in millimeters. The calculation domain is divided into macro-elements for the calculation of temperature, and each macro-element consists of square cells for the simulation of grain structure evolution. The values of the different parameters used in the computation are listed in Table I.

Due to solidification contraction, air gap may be formed between the metal and mold interface during solidification processes. Thus, a critical part in realistically simulating solidification of ingot is the specification of the thermal boundary conditions at the outer surfaces and the heat transfer coefficient due to air gap formation. In this paper, we follow an approach similar to that has been presented in reference [13]. The detailed characterization of the initial and boundary conditions required to describe the temperature evolution in the ingot is summarized in Table II. The expression for the heat transfer coefficient between the metal and mold interface, presented in Table II, describes the decrease in heat transfer that occurs during cooling due to the air gap formation.

Fig. 4a and b illustrate the effect of the solidification contraction on the cooling curves at the point 1 2 and 3 (as shown in Fig. 3) in the ingot. As indicated in Fig. 4a, the ingot is cooled at a faster rate in comparison with Fig. 4b. This is due to, without consideration of solidification contraction, that no air gap is formed between the metal and mold interface, which enhances heat transfer from the metal to the mold. This suggests that the thermal resistance formed by the air gap may have an important effect on the solidification processes of the ingot.

The time dependence of the metal-mold heat transfer coefficient is shown in Fig. 5, which corresponds to the case of Fig. 4b. However, in the case of Fig. 4a, metal-mold heat transfer coefficient is kept as a constant: $hi = h_{\max} = 1500\ \text{W m}^{-2}\ \text{K}^{-1}$.

An attempt at 2D representation of the distribution of secondary phases in equiaxed alloys is shown in

TABLE I Values of the different parameters used in the computation

Thermo-physical properties of materials			
Material	Density (kg/m^3)	Specific heat (J/kg·K)	Thermal conductivity (W/m·K)
Ti-45 at%Al alloy	3800	887.3	23
A3 steel	7840	386	49.8
Insulating powder	304.4	134.0	0.3201
Other parameters			
$\Delta T_{\max}$ (K)			5
ΔT_σ (K)			1
$n_{\max}$ (m^{-3})			3×10^8
Δx (μm)			200

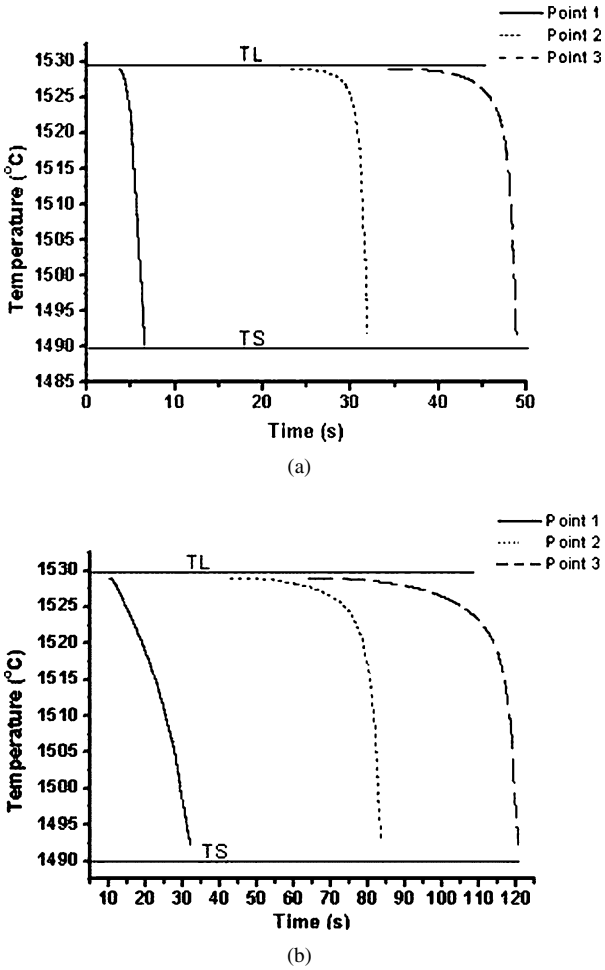

Figure 4 Cooling curves at different positions in the ingot (a) without and (b) with the solidification contraction.

Fig. 6. The white spots represent the last solidified liquid regions, i.e. the last liquid regions prone to peritectic phase formation for Ti-45 at%Al alloy. Usually, peritectic phases form at the boundary of the primary arms of columnar dendrites or at the grain boundary of equiaxed dendrites. As noticed, in Fig. 6, peritectic

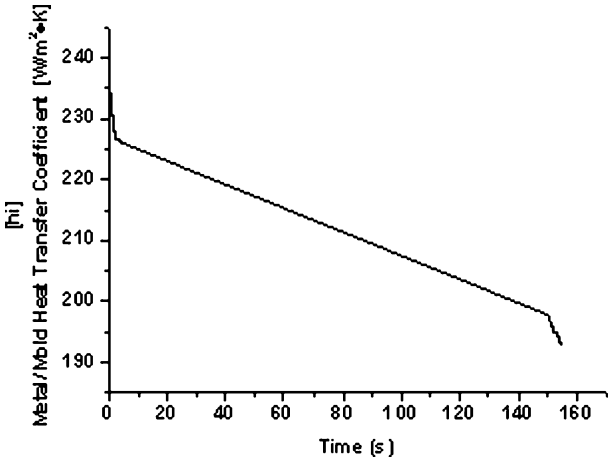

Figure 5 Time dependence of the metal-mold heat transfer coefficient.

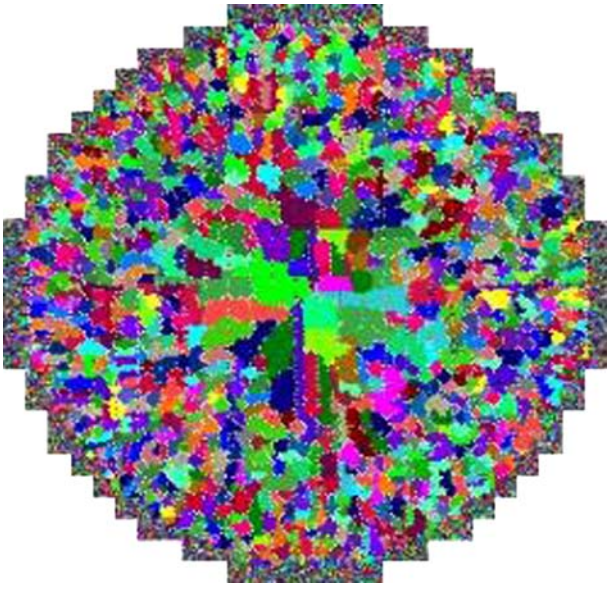

Figure 6 Last solidified liquid regions in solidification of Ti-45 at%Al alloy.

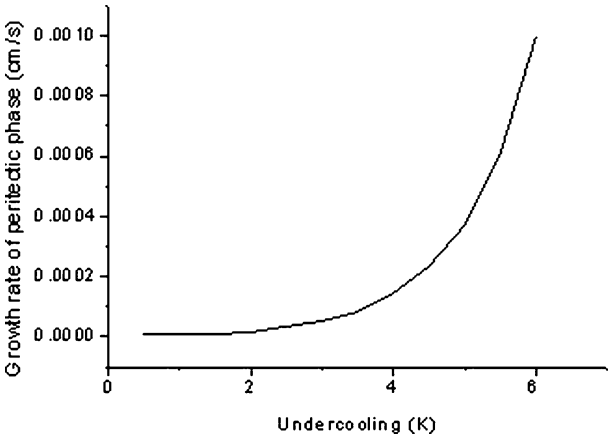

Figure 7 Growth kinetics of peritectic phase, as calculated by peritectic growth kinetics model.

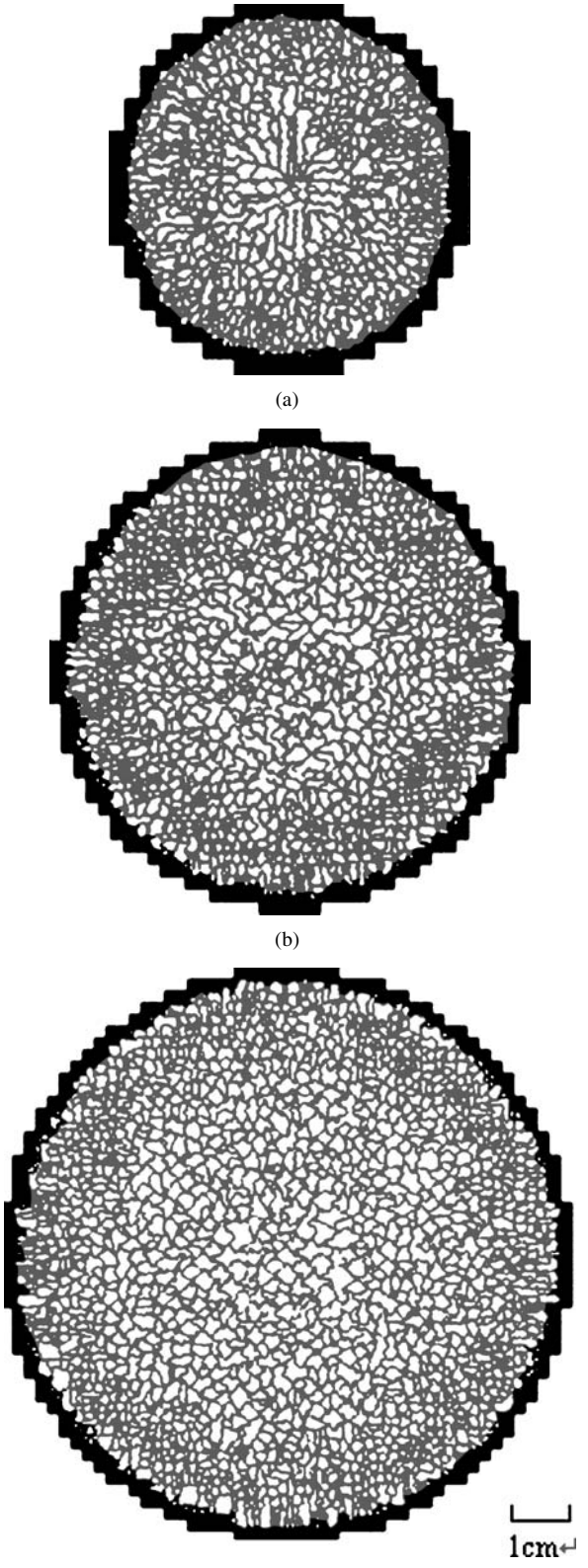

Figure 8 Simulated grain structures of Ti-45 at%Al alloy ingot at three different cross sections: (a) Section A, (b) Section B and (c) Section C.

phases are randomly distributed at the grain boundary of the equiaxed.

Growth rates of peritectic phases formed in the last solidified liquid regions are calculated by peritectic growth kinetics model. And the relationship between the growth rate and undercooling is given by solution of Equation 14. As can be seen in Fig. 7, growth rate increases with an increasing undercooling.

TABLE II Initial and boundary conditions used in the thermal analysis

Initial conditions	
Initial mold temperature	25°C
Pouring temperature	1600°C
Boundary conditions	
Heat loss at the surface of the mold	$Q_{se} = h_{se}(T_{s\_mold} - T_e) + \sigma \varepsilon_m((T_{s\_mold} + 273)^4 - (T_e + 273)^4)$
	$h_{se} = 10\ \text{W m}^{-2}\ \text{K}^{-1} \quad T_e = 25°\text{C} \quad \varepsilon_m = 0.64$
	$\sigma = 5.67 \times 10^{-8} \text{W m}^{-2}\ \text{K}^{-4}$
Heat transfer between the metal and mold interface (This expression includes conduction, radiation, and gap formation due to solidification contraction.)	$Q_{cm} = h_r(T_{mold} - T_{metal})$
	$h_r = h_{conduction} + (1 - f_L)\, h_{radiation}$
	$h_{conduction} = h_{min} + f_L(h_{max} - h_{min})$
	$h_{radiation} = \sigma \varepsilon_{cm}((T_{mold} + 273)^2 + (T_{metal} + 273)^2)((T_{mold} + 273) + (T_{metal} + 273))$
	$h_{min} = 20\ \text{W m}^{-2}\ \text{K}^{-1}$
	$h_{max} = 1500\ \text{W m}^{-2}\ \text{K}^{-1}$
	$\varepsilon_{cm} = 0.72$
	$f_L = \begin{cases} 1 & \text{if } T_{metal} > TL \\ \frac{TL - T_{metal}}{TL - TS} & \text{if } TS < T_{metal} < TL \\ 0 & \text{if } T_{metal} < TS \end{cases}$

As the thickness of the mold wall (TMW) directly affects the cooling rate of the local part, it affects the grain size. As the TMW increases, finer microstructure is formed. Three typical cross sections with different TMW are selected for simulation, as shown in Fig. 3. Fig. 8 indicates the simulated grain structures. It can be observed that increasing the TMW, higher cooling rate in section A leads to more effective nucleation that results in the formation of the finer microstructure in comparison with section B and C. In Table III, the calculated and observed average grain sizes are compared.

TABLE III The calculated and observed average grain sizes at three sections

Section	TMW (mm)	Calculated average radius of equiaxed grains (mm)	Experimental results (mm)
A	46	0.75	0.7
B	30	1.01	1.12
C	20	1.1	1.3

Taking into account the solidification contraction during solidification processes, the present stochastic model gives the grain structure shown in Fig. 9b. As can be seen, with the formation of a shrinkage cavity at the top part of the ingot, the grain structure is fully equiaxed and is much closer to the experimental observation shown in Fig. 10. The change in the final grain morphology can be better understood by the formation of air gap between the metal and mold interface. Fig. 9a indicates that a good wettability at the metal and mold interface enhances heat transfer and causes a larger temperature gradient in the liquid, which favors the columnar grain growth and delays the columnar to the equiaxed transition. And when the equiaxed grains begin to grow in front of the columnar ones, the structures remain equiaxed with a slightly elongated

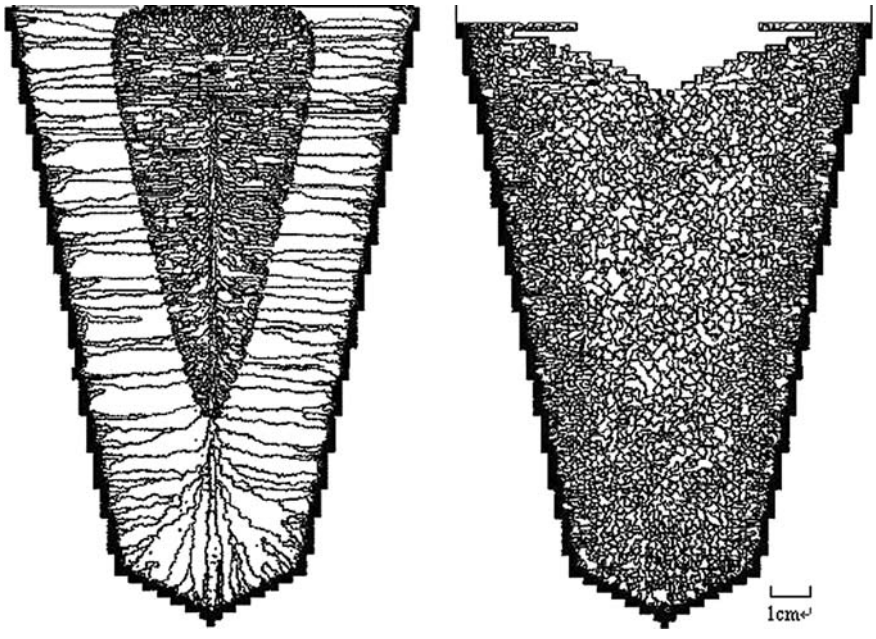

Figure 9 Simulated grain structures of Ti-45 at%Al alloy ingot at the vertical section: (a) without and (b) with the solidification contraction.

Figure 10 Experimental solidification grain structure of Ti-45 at%Al alloy ingot at the vertical section.

morphology due to a strong thermal gradient in the liquid. When considering the air gap formation, temperature gradient in the liquid may decrease due to a decrease in the metal-mold heat transfer coefficient and thus, the CET may easily occur.

6. Conclusions

A comprehensive stochastic model for simulating grain structure formation and evolution has been developed, based on a finite differential method (FDM) for macroscopic heat flow calculation and a cellular automaton method (CA) for microscopic modelling of nucleation, growth, solute redistribution and solute diffusion. For Ti-45 at%Al alloy, the formation of peritectic phases in the last solidified liquid regions is considered. The growth rates of peritectic phases are calculated by peritectic growth kinetics model. The solidification contraction is also taken into account. The simulated results are in good agreement with those obtained experimentally. It is found that the present stochastic model can be successfully applied to predict the grain structure formation and evolution during solidification processes.

Acknowledgements

Authors would like to thank the National Natural Science Foundation of China (50395102) and the Distinguished Young Foundation of Heilongjiang Province (Jc-02-10) for their financial support.

References

1. C. Y. WANG and C. BECKERMANN, *Metall. Trans.* A. **24** (1993) 2787.
2. CH.-A. GANDIN, CH. CHARBON and M. RAPPAZ, *ISIJ.* **35** (1995) 651.
3. J. A. SPITTLE and S. G. R. BROWN, *Acta Metall.* **37** (1989) 1803.
4. M. RAPPAZ and CH.-A. GANDIN, *Acta Metall.* **41** (1992) 345.
5. LAURENTIU NASTAC and DORU M. STEFANESCU, *Modell. Simul. Mater. Sci. Eng.* **5** (1997) 391.
6. L. NASTAC and DORU M. STEFANESCU, *Metall. Trans.* A. **27** (1996) 4061.
7. TONGMIN WANG, JUNZE JIN, XIANSHU ZHENG and ITSUO OHNAKE, *Int. J. Cast Metals Res.* **15** (2002) 231.
8. W. KURZ, B. GIOVANOLA and R. TRIVEDI, *Acta Metall.* **34** (1986) 823.
9. H. W. KERR and W. KURZ, *Inter. Mater. Rev.* **41** (1996) 129.
10. Y. Q. SU, C. LIU, X. Z. LI, J. J. GUO, B. S. LI, J. JIA and H. Z. FU, *Intermetallics* **13** (2005) 267.
11. J. P. GU and C. BECKERMANN, *Metall. Trans.* A. **30** (1999) 1357.
12. CH.-A. GANDIN and M. RAPPAZ, *Acta Metall.* **42** (1994) 2233.
13. A. JACOT, D. MAIJER and S. COCKCROFT, *Metall. Trans.* A **31** (2000) 2059.

Received 12 October 2004
and accepted 7 March 2005